AGU PUBLICATIONS

JGR

Journal of Geophysical Research: Space Physics

RESEARCH ARTICLE

10.1002/2016JA023657

Key Points:

- We connect in situ electric field measurements to slot region flux enhancements for 100s keV electrons
- An increase in convection can explain enhancements for electrons up to 500 keV near $L = 3$ through inward radial transport
- Our convection model does not match higher-energy flux observations, indicating a transition point where other mechanisms are required

Correspondence to:
S. Califf,
califf@colorado.edu

Citation:
Califf, S., X. Li, H. Zhao, A. Kellerman, T. E. Sarris, A. Jaynes, and D. M. Malaspina (2017), The role of the convection electric field in filling the slot region between the inner and outer radiation belts, *J. Geophys. Res. Space Physics*, *122*, doi:10.1002/2016JA023657.

Received 6 NOV 2016
Accepted 14 FEB 2017
Accepted article online 19 FEB 2017

©2017. American Geophysical Union. All Rights Reserved.

The role of the convection electric field in filling the slot region between the inner and outer radiation belts

S. Califf[1], X. Li[1], H. Zhao[1], A. Kellerman[2], T. E. Sarris[3], A. Jaynes[1], and D. M. Malaspina[1]

[1]Laboratory for Atmospheric and Space Physics, University of Colorado Boulder, Boulder, Colorado, USA, [2]Department of Earth, Planetary and Space Sciences, University of California, Los Angeles, California, USA, [3]Department of Electrical Engineering, Democritus University of Thrace, Xanthi, Greece

Abstract The Van Allen Probes have reported frequent flux enhancements of 100s keV electrons in the slot region, with lower energy electrons exhibiting more dynamic behavior at lower L shells. Also, in situ electric field measurements from the Combined Release and Radiation Effects Satellite, Time History of Events and Macroscale Interactions during Substorms (THEMIS), and the Van Allen Probes have provided evidence for large-scale electric fields at low L shells during active times. We study an event on 19 February 2014 where hundreds of keV electron fluxes were enhanced by orders of magnitude in the slot region and electric fields of 1–2 mV/m were observed below $L = 3$. Using a 2-D guiding center particle tracer and a simple large-scale convection electric field model, we demonstrate that the measured electric fields can account for energization of electrons up to at least 500 keV in the slot region through inward radial transport.

1. Introduction

Recent observations by the Magnetic Electron Ion Spectrometer (MagEIS) [*Blake et al.*, 2013] on board the Van Allen Probes have highlighted the dynamic nature of 100s keV electrons at low L shells ($L < 3.5$) in the inner magnetosphere [e.g., *Zhao et al.*, 2014; *Turner et al.*, 2015; *Reeves et al.*, 2016]. The quiet time structure of the radiation belts consists of an inner belt ($L < \sim 2.5$), an outer belt ($L > \sim 3.5$), and a slot region ($\sim 2.5 < L < \sim 3.5$) that contains fewer energetic electrons. The structure of the slot region is energy dependent, with the outer edge of the inner belt extending to larger L shells for lower energies. Frequently during storms, the hundreds of keV electron flux increase by orders of magnitude at low L shells ($L < 3$), sometimes filling the slot region to the point that there is no clear distinction between the inner and outer belts.

Figure 1 shows MagEIS spin-averaged electron fluxes for energies between 169 and 731 keV sorted by L shell from 15 May 2013 to 15 October 2014. For electron flux plots in this study, we use McIlwain L computed from the OP77 magnetic field model, which is provided in the MagEIS level 2 and level 3 data. The outer radiation belt is more dynamic than the inner belt, and the inner belt is mostly composed of relatively lower energy electrons. Many of the variations in the outer belt extend to $L = 3$ or below, and some enhancements appear to connect the inner and outer belts, filling the slot region. These slot-filling events occur frequently for lower energies but become much less common for electrons above ~500 keV.

Spin-averaged fluxes for 169–731 keV electrons at specific L shells are plotted for a series of events between 15 June 2013 and 15 November 2013 in Figure 2. Flux enhancements of an order of magnitude or more are common at $L = 3$ for 169 keV electrons, and the flux is more variable at higher L shells. The enhancements are characterized by a fast rise phase followed by a slow decay: the rise phase corresponds to the period where the energization mechanism is dominating loss, and the decay is likely caused by slow pitch angle scattering from plasmaspheric hiss [e.g., *Lyons and Thorne*, 1973].

We are focused on electric fields during the rise phase of the enhancements in order to investigate the mechanism that is energizing 100s keV electrons at low L shells. Radiation belt electron energization is typically discussed in terms of radial transport and local acceleration. If a particle is transported radially inward and the first adiabatic invariant is conserved, the particle will gain energy as the magnetic field strength increases. The electric field is important in this scenario because inward radial transport across magnetic field lines requires an azimuthal electric field.

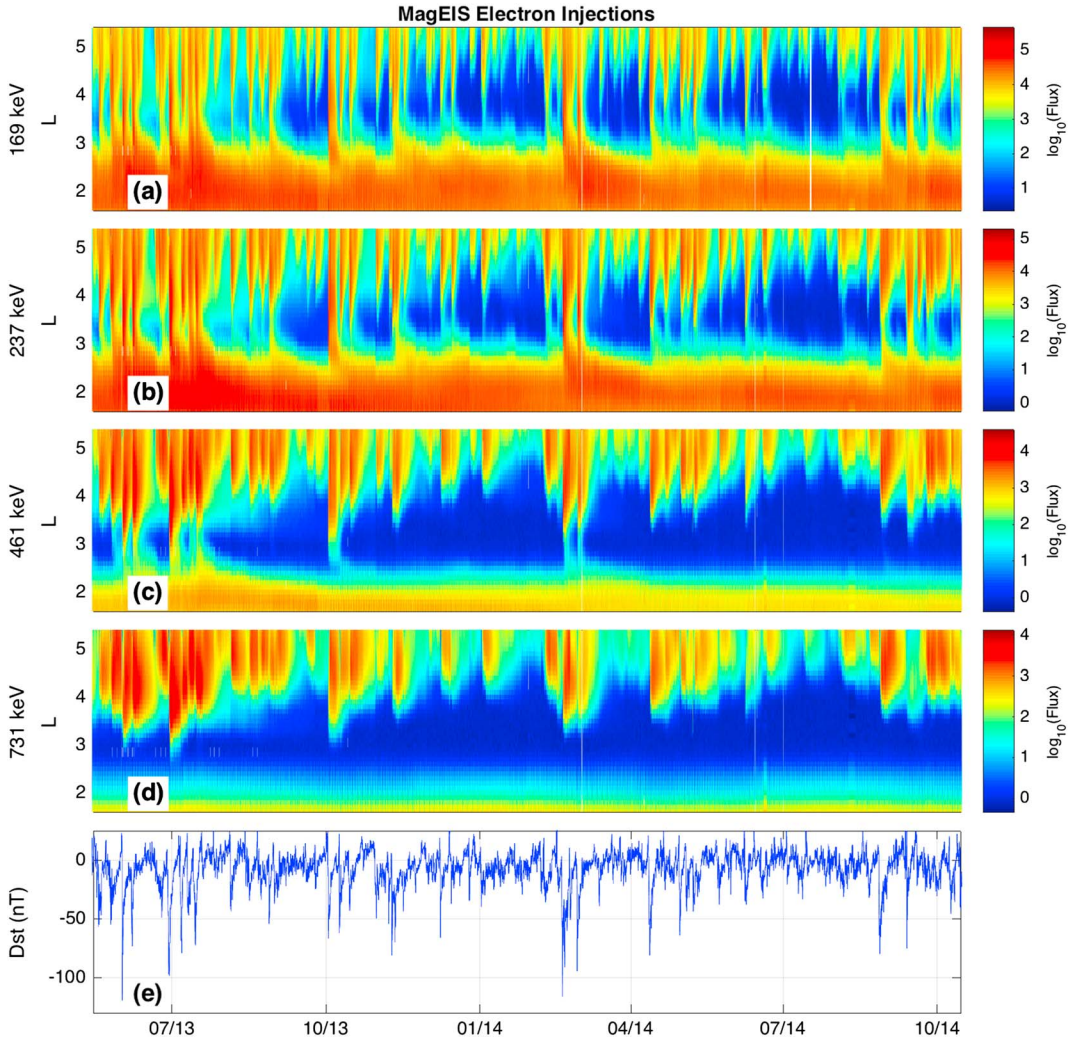

Figure 1. Spin-averaged fluxes for electrons between (a–d) 169 and 731 keV measured by both Van Allen Probes and (e) the *Dst* index from 15 May 2013 to 15 October 2014.

Local acceleration by chorus has been identified as a mechanism for energizing electrons to MeV energies [e.g., *Reeves et al*., 2013], but there is ongoing debate over the effect chorus may have on 100s keV electrons. Some authors expect chorus to primarily cause loss for 100s keV electrons [e.g., *Shprits et al*., 2008], while others have attributed hundreds of keV electron enhancements to acceleration by chorus [e.g., *Thorne et al*., 2007].

In situ measurements by CRRES, Time History of Events and Macroscale Interactions during Substorms (THEMIS), and the Van Allen Probes have demonstrated that large-scale electric fields of up to a few mV/m can exist below $L = 3$ during storms [e.g., *Rowland and Wygant*, 1998; *Califf et al*., 2014, 2016; *Thaller et al*., 2015]. Some of the mechanisms that can generate enhanced electric fields deep within the inner magnetosphere include penetration electric fields, subauroral ion drifts, subauroral polarization streams, substorm injections, and interplanetary shocks. The purpose of this study is to investigate the relationship between hundreds of keV electron enhancements in the slot region and large-scale electric fields at low L shells.

Recently, *Su et al*. [2016] modeled inner belt electrons under the influence of various *Kp*-driven electric field models for the 17 March 2013 storm. They found that the low *L* electric fields required to reproduce observed flux enhancements at $L = 1.5$ were stronger than any existing model. That study applied a 2-D guiding center code to electrons with $\mu = 2.5$ MeV/G and $K = 0.3\,R_E G^{1/2}$, which roughly corresponds to 350 keV at $L = 1.5$ and 35 keV at $L = 4.4$. *Selesnick et al*. [2016] also showed that rapid injections of 100s keV electrons below

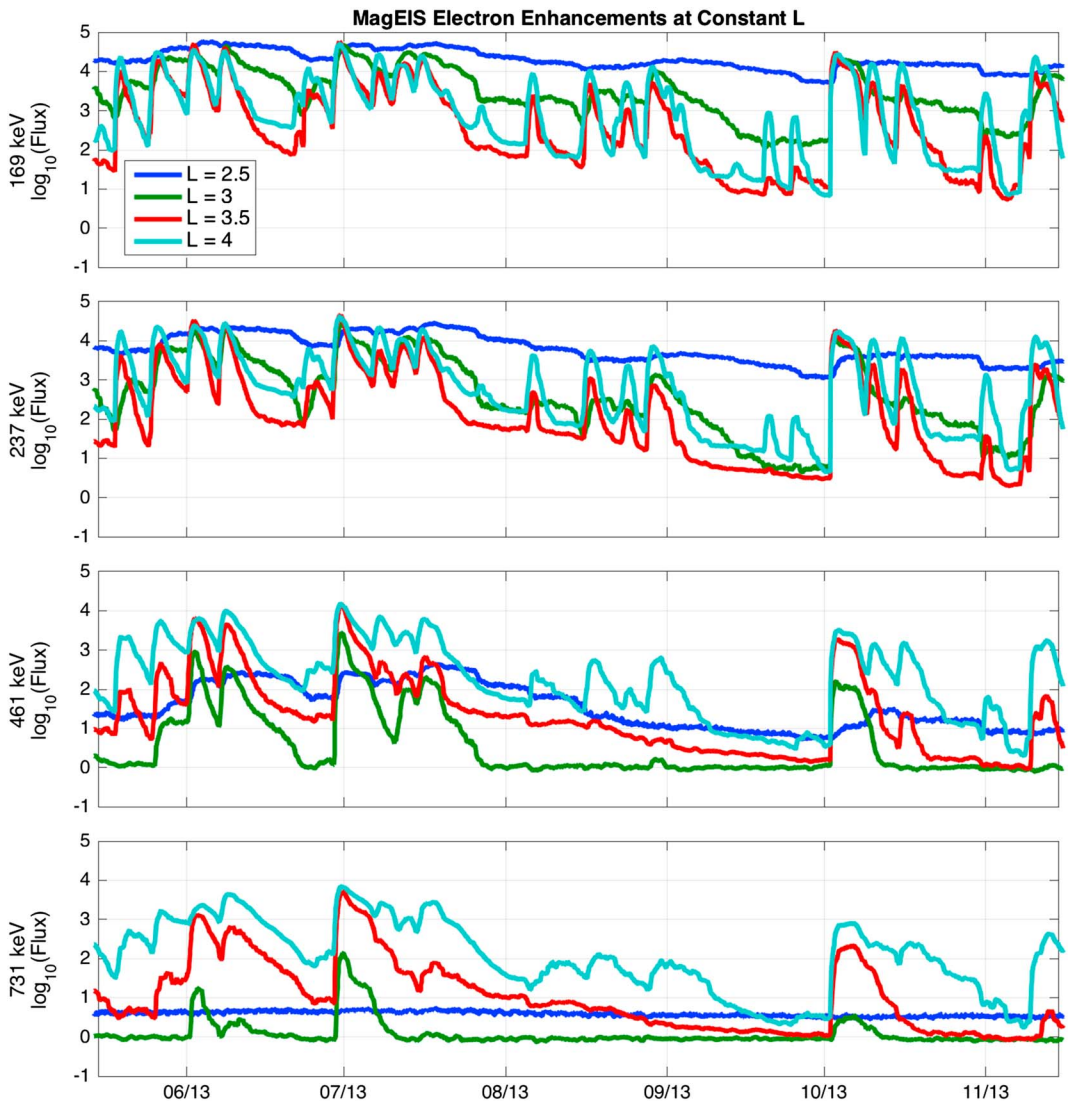

Figure 2. Spin-averaged fluxes at specific L shells from June to November 2013 smoothed with a 1 day moving average.

$L = 2$ during the 22–23 June 2015 storm could be caused by a 5 mV/m convection electric field; however, they were unable to verify this electric field with in situ measurements due to uncertainties related to $\mathbf{v} \times \mathbf{B}$ subtraction near perigee.

We study an event on 19 February 2014 where flux enhancements for 100s keV electrons were observed below $L = 3$ by the Van Allen Probes. Electric field and plasmapause measurements by the Van Allen Probes and THEMIS E provide direct evidence of large-scale electric fields at low L shells during the event. We model the evolution of electron phase space density (PSD) over a range of energies using a 2-D guiding center particle tracer and a simple uniform dawn-to-dusk electric field to demonstrate that the observed electric fields are sufficient to explain the slot region electron enhancements.

2. Event Overview

On 18 February 2014, the interplanetary magnetic field (IMF) turned southward, initiating a geomagnetic storm with minimum $Dst = -116$ nT. The main phase of the storm was separated into two phases: *Dst* began to recover near 02 UT on 19 February 2014 and then an abrupt increase in solar wind speed and further southward turning of the IMF due to a coronal mass ejection extended the main phase until the IMF turned sharply northward at 08 UT. Large flux enhancements for 100s keV electrons were observed in the slot region

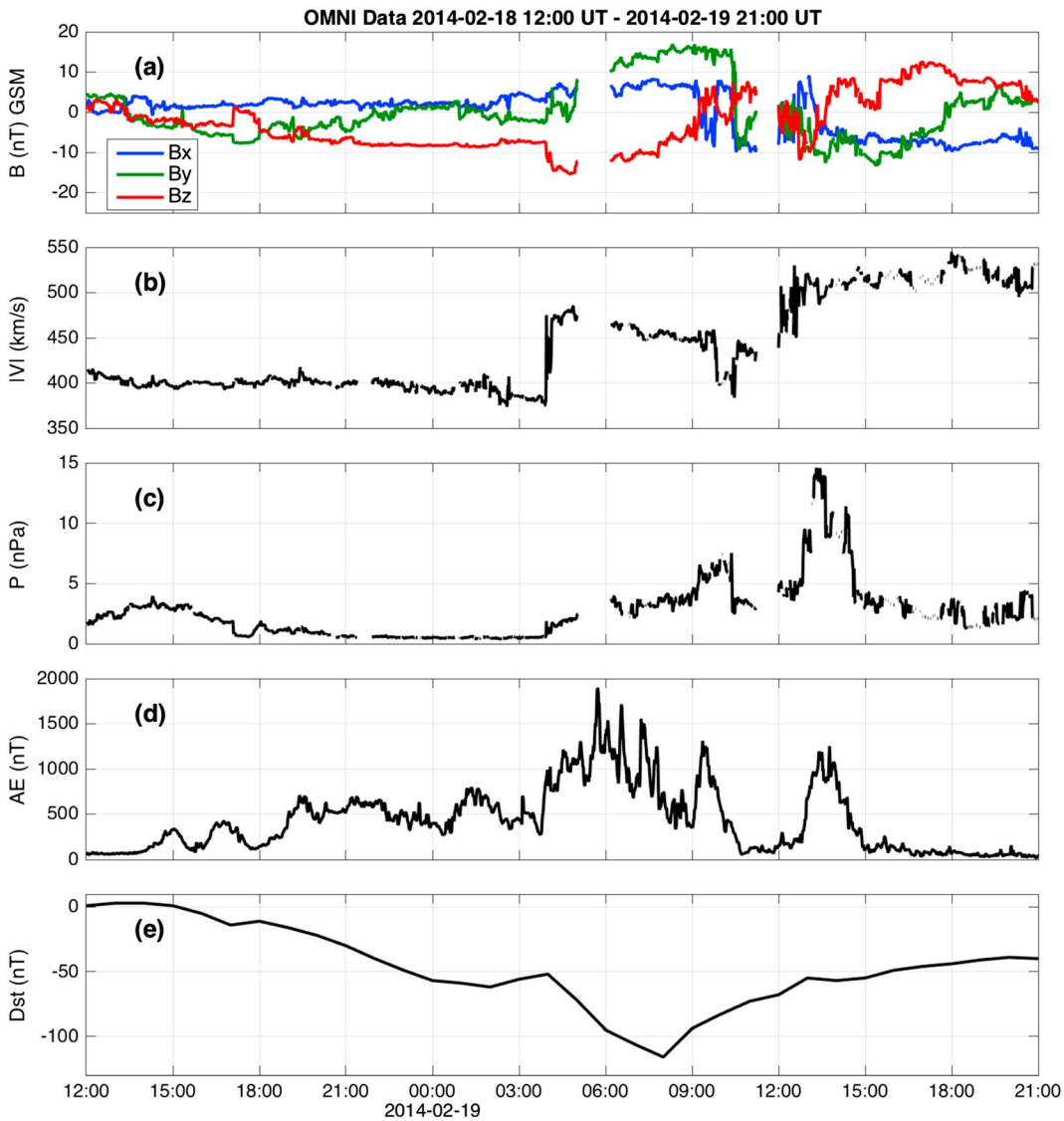

Figure 3. Solar wind data and geomagnetic indices for the 19 February 2014 geomagnetic storm. (a) Interplanetary magnetic field, (b) solar wind speed, (c) flow pressure, (d) *AE* index, and (e) *Dst* index.

at the beginning of the recovery phase. Figure 3 shows the solar wind data and geomagnetic indices during this storm.

Spin-averaged electron fluxes observed by the Van Allen Probes over the course of the event are shown in Figure 4. Flux is plotted against L shell, and the time of each observation is displayed in color. Flux enhancements of more than 2 orders of magnitude were observed for electrons with energies below 350 keV at $L = 3$, and 900 keV electrons were enhanced near $L = 3.5$. The initial observations (blue lines) display a typical inner belt, outer belt, and slot region structure, with the outer edge of the inner belt extending to larger L shells for lower energies. During the enhancement, the inner edge of the outer belt moved earthward over the course of ~10 h until the outer belt effectively merged with the inner belt for energies below 350 keV. The apparent gradual inward movement of the inner edge of the outer belt is common in slot-filling events.

3. Flux and Phase Space Density (PSD) Evolution

We have identified two outbound Van Allen Probes passes on 19 February 2014 where the hundreds of keV electron flux increased by more than an order of magnitude at low L shells over ~1.5 h. In order to evaluate

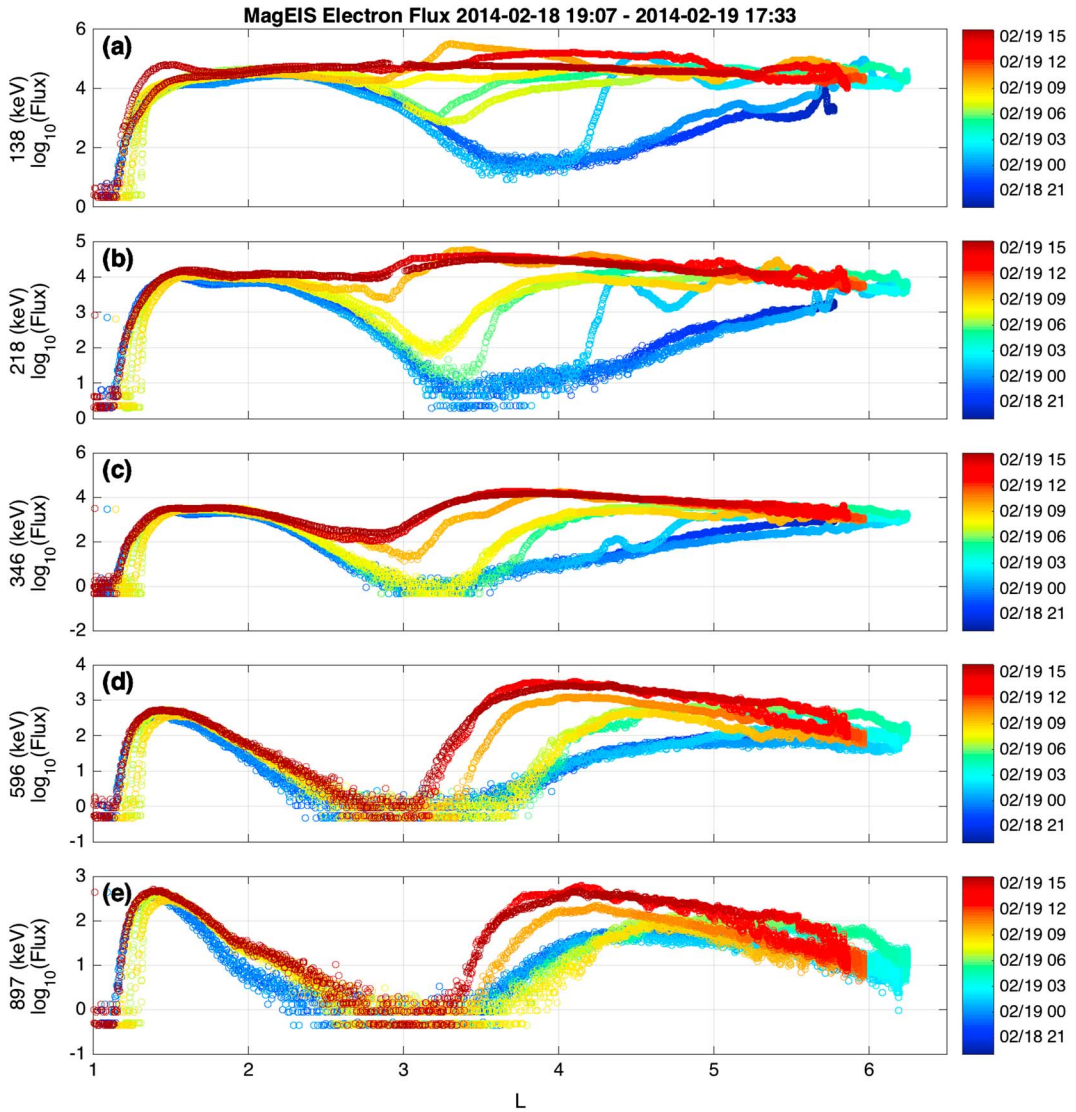

Figure 4. Spin-averaged electron flux profiles sorted by L shell during the 19 February 2014 geomagnetic storm for (a) 138 keV, (b) 218 keV, (c) 346 keV, (d) 596 keV, and (e) 897 keV. Time is plotted in color.

the relationship between large-scale electric fields and the electron dynamics, we converted flux to PSD as a function of the three adiabatic invariants, μ, K, and L^* [e.g., *Green and Kivelson*, 2004]. A 100 keV equatorially mirroring electron corresponds to $\mu = 10$ MeV/G at $L = 3$ in a dipole field, and if μ is conserved, the energy would be 14 keV for the same electron at $L = 6$. Therefore, complete radial profiles ($L \sim 2$–6) for lower μ values require combined data from the Helium, Oxygen, Proton, and Electron Mass Spectrometer (HOPE) (1 eV to 50 keV) [*Funsten et al.*, 2013] and MagEIS (30 keV to 4.8 MeV).

The flux data are provided at fixed pitch angles and energies, which do not correspond to fixed μ and K. In order to create profiles for constant μ and K, multiple levels of interpolation were required. First, measured fluxes at each pitch angle were converted to PSD for each energy channel. This resulted in a PSD distribution for each pitch angle corresponding to an irregular grid in μ. We defined μ based on the measured magnetic field. Next, we interpolated the PSD to a constant μ grid at each pitch angle. This step was performed separately for HOPE and MagEIS because the level 3 data for the two instruments are provided at different pitch angle intervals. At this point, we have PSD at a constant μ grid for specific pitch angles that do not map to a fixed K grid. Next, we computed a set of pitch angles using the TS04 magnetic field model [*Tsyganenko and*

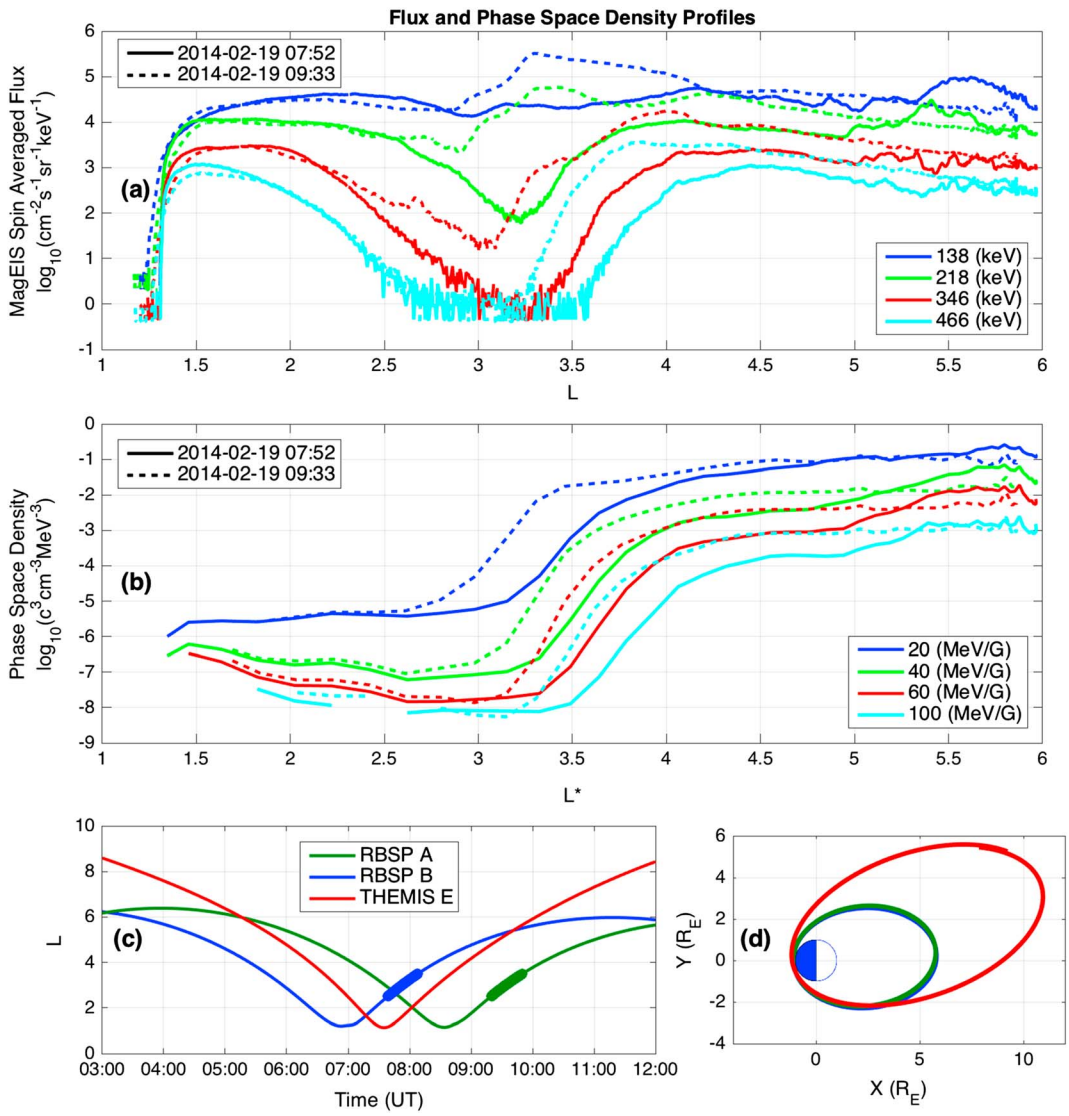

Figure 5. (a) Spin-averaged flux and (b) PSD evolution between successive outbound Van Allen Probes passes on 19 February 2014. The (c) *L* sampling and (d) orbits projected into the GSE *XY* plane for the Van Allen Probes and THEMIS E.

Sitnov, 2005] corresponding to a fixed grid of K values and then interpolated the PSD for each μ to the computed pitch angles at each time step, resulting in PSD for fixed μ and *K* over the entire orbit.

After interpolating the PSD to constant μ and *K*, we chose values for μ and *K* that have complete coverage across L shells for both passes. $K = 0$ ($G^{1/2}R_E$) corresponds to equatorially mirroring particles, which cannot be measured when the spacecraft is located off the magnetic equator. We selected $K = 0.1$ ($G^{1/2}R_E$) to obtain complete radial PSD profiles, which corresponds to electrons with equatorial pitch angles of ~45°.

Figure 5 shows the electron flux and PSD profiles measured by the two Van Allen Probes. Flux is plotted against McIlwain *L*, and PSD is plotted against *L**. Van Allen Probe B passed $L = 3$ at 07:52 UT, and Van Allen Probe A passed $L = 3$ at 09:33 UT. The minimum hourly *Dst* of −116 nT was recorded at 08:00 UT, so these observations occur near the beginning of the recovery phase of the storm. The flux profiles exhibit a large increase below $L = 3$ for electrons up to 350 keV between the two passes.

The PSD profiles in Figure 5b correspond to roughly the same energies as the fluxes in Figure 5a for 90° pitch angle electrons at $L^* = 3.5$. When sorted by PSD coordinates, the enhancements appear to be more organized, with a sharp gradient in PSD that moves radially inward between consecutive outbound passes.

Growing local peaks in PSD have been used to identify local acceleration processes [e.g., *Green and Kivelson*, 2004]. The absence of local peaks and the similar shape of the radial PSD profiles between passes in Figure 5b suggests that the flux enhancements in Figure 5a were caused by inward radial transport.

The PSD profiles in Figure 5 show a steep radial gradient that is located at higher L for higher μ. Between observations separated by ~1.5 h, the location of the steep PSD gradient moves inward by ~0.3 L. This demonstrates that a relatively small inward displacement of the preexisting electron population can create a dramatic change in the flux profile, especially in the slot region where fluxes are initially low. The PSD profiles suggest inward transport as a mechanism, raising the question, were there enhanced electric fields in the slot region that could have transported the electrons?

4. Electric Field and Plasmapause Observations

The flux enhancements near $L = 3$ under study occurred between 07:52 UT and 09:33 UT on 19 February 2014, which correspond to an outbound Van Allen Probe B and an outbound Van Allen Probe A pass, respectively. The Van Allen Probes crossed through $L = 3$ near dusk on the inbound pass and dawn on the outbound pass. Between the flux enhancement observations, THEMIS E passed through the inner magnetosphere across similar local times as the Van Allen Probes, providing an additional set of electric field measurements. The Van Allen Probes and THEMIS E orbits are shown in Figure 5d along with the times of inbound and outbound L sampling (Figure 5c) for each spacecraft on 19 February 2014.

Figure 6 shows data from both Van Allen Probes on inbound duskside passes prior to the flux enhancement. Beginning at ~04 UT, Van Allen Probe B observed an elevated dawn-dusk ($+E_y$) electric field of approximately 1 mV/m spanning from $L = 6$ to below $L = 2$ on the duskside (blue line, Figure 6a). Measurements from Van Allen Probe A, which was trailing Van Allen Probe B by ~1.5 h, display similar duskside electric fields until at least 08 UT (green line, Figure 6a). There are variations on top of an average positive E_y, with larger variations at higher L shells. The electric field data were provided by the Electric Field and Waves (EFW) instrument [*Wygant et al*., 2013], and spacecraft $\mathbf{v} \times \mathbf{B}$ and the corotation electric field have been subtracted, leaving the electric field in the frame corotating with Earth. The modified geocentric solar ecliptic (MGSE) coordinate system is defined by the spacecraft spin configuration and is similar to geocentric solar ecliptic (GSE) coordinates: MGSE Y lies in the spin plane and is approximately aligned in the dawn-to-dusk direction.

At ~04 UT, the plasmapause can be inferred to be located near $L = 5.8$ by both the radial gradient in spacecraft potential (and density) (blue lines, Figures 6b and 6c) and the presence of plasmaspheric hiss (Figure 6d) measured by Van Allen Probe B, which is identified by the broadband wave power between 100 and 1000 Hz [*Malaspina et al*., 2015]. The variations in spacecraft potential beyond $L = 5.8$ may be due to a plasmaspheric plume, which is often observed on the duskside during active times and is a consequence of increased convection in the inner magnetosphere [e.g., *Darrouzet et al*., 2008]. The density (Figure 6c) is derived from spacecraft potential [*Kurth et al*., 2015], and the spectral data (Figure 6d) are combined from the Electric and Magnetic Field Instrument Suite and Integrated Science (EMFISIS) Waveform Receiver (WFR) (10 Hz to 12 kHz) and High-Frequency Receiver (HFR) (10 to 500 kHz) [*Kletzing et al*., 2013]. Approximately 1.5 h later, Van Allen Probe A passed though the duskside inner magnetosphere, and similar 1 mV/m electric fields were observed extending to low L shells with more variation at higher L shells (green line, Figure 6a).

Figure 7 displays the consecutive outbound Van Allen Probes passes on the dawnside that revealed a large increase in flux for 100s keV electrons in the slot region. Both spacecraft measured small positive or possibly even negative quasi-static electric fields across most of the dawnside, in contrast to the positive 1 mV/m dawn-dusk electric fields on the duskside. Similar dawn-dusk asymmetry in the electric field with stronger electric fields near dusk has been reported in statistical data during active times [e.g., *Califf et al*., 2014].

The data in Figure 7 show a dramatic difference in the plasmapause location compared to the previous inbound pass on the duskside (Figure 6). The extended plasmasphere on the duskside is caused by combination of convection and corotation electric fields, which act against each other near dusk, causing the Alfven boundary for cold plasma to move to larger L shells [e.g., *Carpenter et al*., 1993]. The gradient in spacecraft potential (and density) indicates that the plasmapause was located near $L = 2.2$ at 07:30 UT, and was below

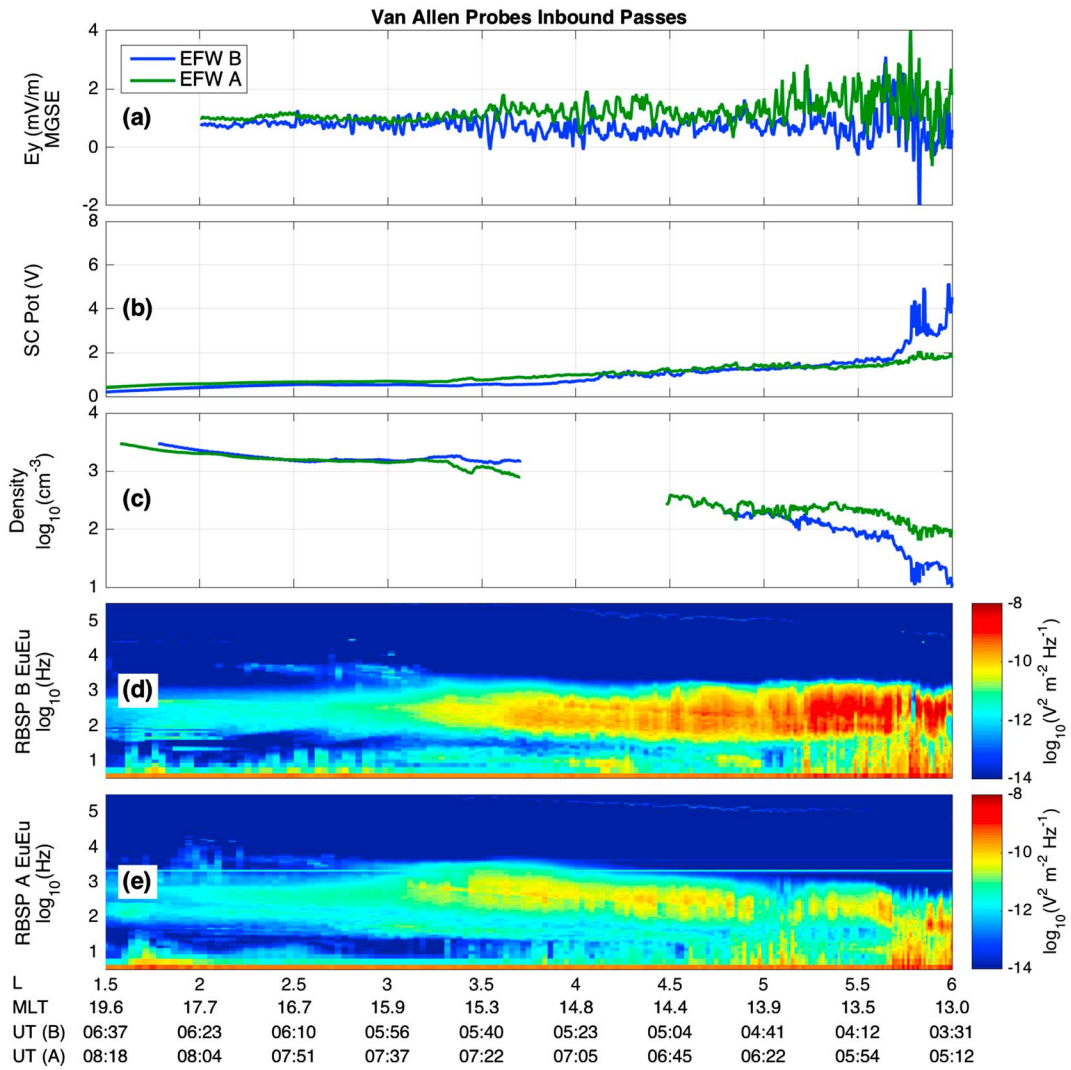

Figure 6. Inbound passes for both Van Allen Probes sorted by L shell (UT increases from right to left). (a) Electric field MGSE *Y* measurement in the frame corotating with Earth, (b) spacecraft potential, (c) density derived from spacecraft potential, (d) combined EMFISIS WFR and HFR electric field wave power from Van Allen Probe B, and (e) electric field wave power from Van Allen Probe A.

$L = 2$ at 09 UT (Figures 7b and 7c). This interpretation is also supported by the lack of plasmaspheric hiss outside of $L = 2$, the existence of chorus (~10 kHz) starting at $L = 2$ and the broadband electrostatic waves below 100 Hz. Chorus waves can only propagate efficiently outside the plasmapause, and broadband electrostatic waves have been associated with the plasmapause boundary [*Malaspina et al.*, 2015].

The dynamics of the plasmasphere are driven by large-scale electric fields [e.g., *Goldstein et al.*, 2003], so the inward motion of the plasmapause to $L < 2$ provides further evidence of enhanced large-scale electric fields extending to low L shells. If we assume that the plasmapause moved steadily from $L = 2.2$ at 07:30 UT to $L = 1.9$ at 09:00 UT, we can estimate the electric field. At $L = 2$, the magnetic field is approximately 3875 nT assuming a dipole, and an electric field of 1.4 mV/m would be required to move the plasmapause by 0.3 R_E in 1.5 h, which is consistent with the in situ electric field observations.

Electric field measurements by the spacecraft only occur at specific local times, and the radial profile is sampled over hours, so these measurements alone cannot definitively distinguish between localized and large-scale features in time and space. However, when placed in the context of statistical electric field measurements [e.g., *Califf et al.*, 2014], the in situ measurements suggest a large-scale convection pattern across a

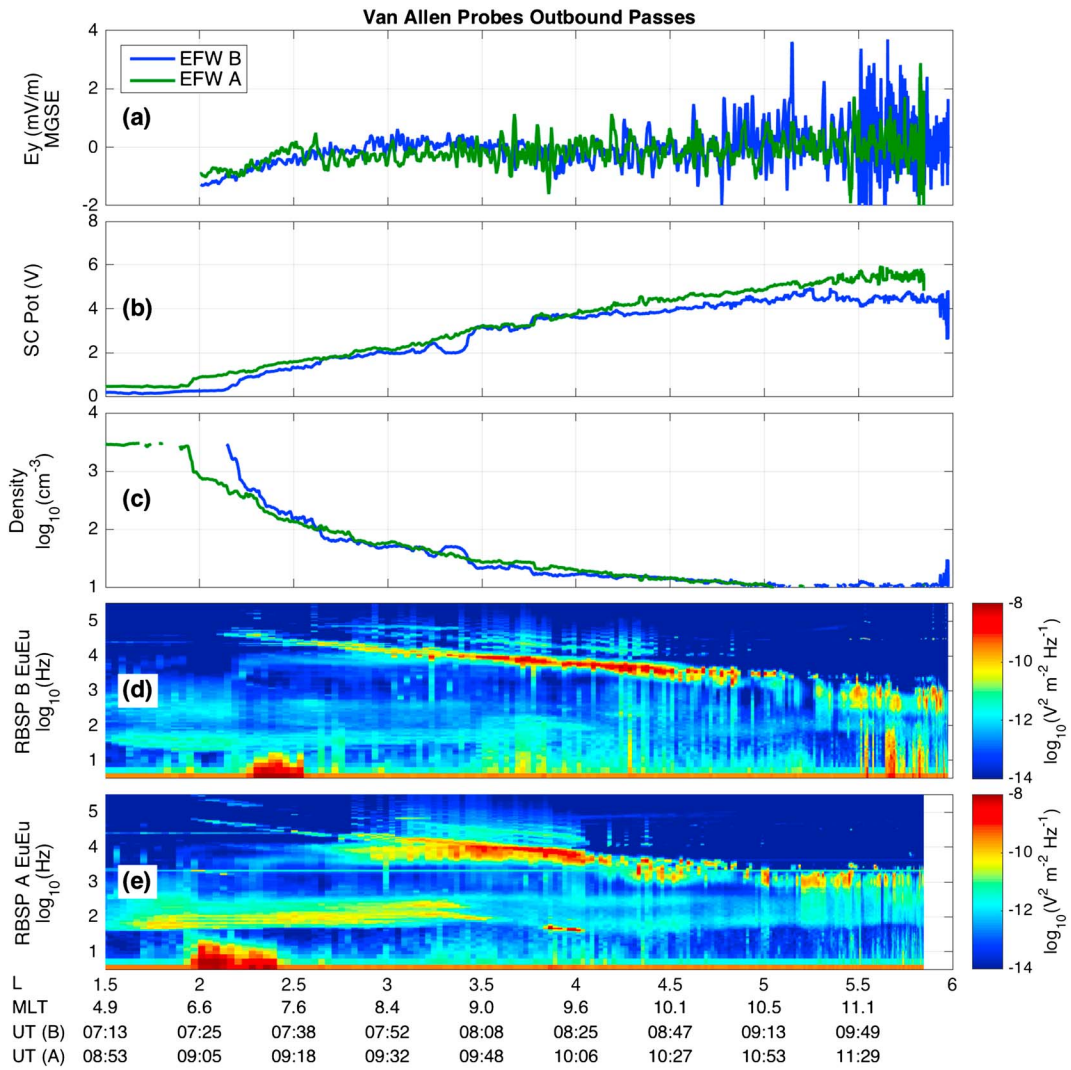

Figure 7. Outbound passes for both Van Allen Probes sorted by L shell in the same format as Figure 6 except that UT increases from left to right.

wide range of L shells persisting for at least 1.5 h, and the plasmapause observations add confidence to this interpretation. Inward plasmapause motion is commonly observed during slot-filling events, suggesting that the electric field responsible for eroding the plasmasphere may also be responsible for transporting 100s keV electrons into the slot region. We identified 35 events between January 2013 and September 2015 where the 200 keV electron flux was observed to increase by more than an order of magnitude at $L = 3$ and the radial flux profiles evolved in a similar manner to those in Figure 4b, filling the slot region over a period of hours. The plasmapause was observed inside $L = 3$ in all of the events except for one, where the minimum plasmapause was measured at $L = 3.25$ on the duskside. The plasmapause was observed at $L = 2.5$ or below in 13 of the 35 events, and most of these plasmapause crossings occurred when the Van Allen Probes were on the dawnside.

Electric field data from THEMIS E are plotted in Figure 8 spanning the time period between the Van Allen Probes electron flux observations. Spin fit data are shown from the Electric Field Instrument in the Despun L-vector Z (DSL) coordinate system with spacecraft $\mathbf{v} \times \mathbf{B}$ and the corotation electric field subtracted [*Bonnell et al*., 2008]. DSL Y points in the dawn-to-dusk direction projected into the spin plane, which is within ~10° of the GSE XY plane. The inbound THEMIS E pass shows a 2 mV/m dawn-dusk electric field across the duskside inner magnetosphere extending below $L = 3$ (Figure 8a) in agreement with the Van Allen Probes

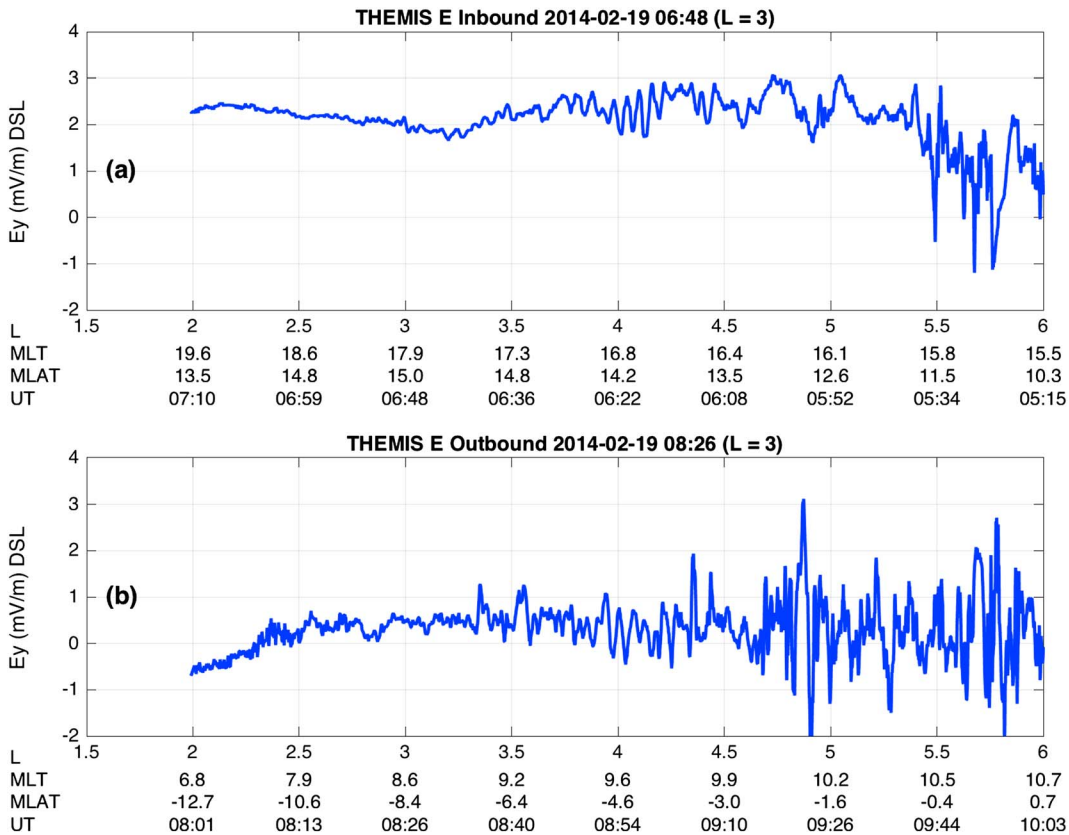

Figure 8. THEMIS E (a) inbound and (b) outbound electric field DSL *Y* measurements surrounding the flux enhancements observed by the Van Allen Probes.

measurements in Figures 6 and 7. Also, the dawn-dusk asymmetry is apparent in the THEMIS E data with electric fields of ~0.5 mV/m on the dawnside outbound pass (Figure 8b).

A negative deviation in E_y of -1 mV/m was observed by THEMIS E and both Van Allen Probes below $L = 2.5$ on the dawnside. There is increased uncertainty in the electric field measurement at low L shells due to $\mathbf{v} \times \mathbf{B}$ subtraction errors. Due to the similar orbital trajectories for the Van Allen Probes and THEMIS E, it is unclear whether these measurements are real or are a result of a common $\mathbf{v} \times \mathbf{B}$ subtraction error between the three spacecraft. Above $L = 3$ the measurements are more reliable: spacecraft $\mathbf{v} \times \mathbf{B}$ is only ~5 mV/m at $L = 3$, and a conservative 5% scale factor error would only introduce 0.25 mV/m $\mathbf{v} \times \mathbf{B}$ subtraction error, which is much smaller than the observations of 1–2 mV/m electric fields.

5. Connection Between the Measured Electric Fields and Electron Flux Enhancements

The PSD profiles in Figure 5 suggest that the slot region flux enhancements were caused by inward radial transport, and the electric field and plasmapause data in Figures 6–8 show that there were 1–2 mV/m electric fields at low L shells during the same time period. Next we evaluate whether these electric fields are capable of transporting 100s keV electrons inward to create the observed flux enhancements.

5.1. Initial Assessment of the Required Versus Measured Electric Fields

If we assume that the electrons moved steadily earthward during the entire 1.5 h interval between observations, we can calculate the electric field required to transport the particles by

$$\boldsymbol{E} = -\boldsymbol{v} \times \boldsymbol{B}. \tag{1}$$

Assuming a dipole magnetic field and a purely azimuthal electric field, an electric field of 0.25 mV/m is needed to move the particles by 0.3 L over 1.5 h at $L = 3.5$, and at $L = 3$, a 0.4 mV/m would be required. The

in situ measurements presented in Figures 6–8 show 1–2 mV/m electric fields inside $L = 3$. The required electric fields are also reasonable given the typical electric field measurements during storms: statistical averages show that there can be ~0.5 mV/m below $L = 3$ during moderate storms, and the electric field can be as large as a few mV/m during the strongest storms [e.g., *Califf et al.*, 2014]. It is also possible that the electron PSD profile changed more abruptly during a short interval between observations, so these estimates are a lower limit for the electric field required to transport the electrons.

5.2. Quantitative Modeling Based On a Simple Convection Electric Field Model

We developed a particle tracer to test the idea that a simple enhancement in the large-scale convection electric field could cause the observed inward transport for 100s keV electrons in the slot region. Radiation belt electrons are not normally associated with the convection electric field because high-energy electrons drift around the Earth relatively quickly (e.g., a 1 MeV electron at $L = 6.6$ drifts in 10 min), so slow changes in the large-scale potential structure have little net effect on the radial location. Radial transport for MeV electrons is typically related to ULF oscillations (f = 1 mHz to 1 Hz) [e.g., *Elkington et al.*, 2003] or inductive electric fields from interplanetary shocks [e.g., *Li et al.*, 1993]. Lower energy electrons (100 s keV) have drift periods on the order of an hour, so it is conceivable that slower changes in large-scale electric fields could play an important role in their dynamics.

The particle tracer applies a 2-D guiding center approximation under a uniform dawn-dusk electric field to model the drift paths of equatorially mirroring electrons assuming a static dipole magnetic field. The guiding-center velocity is given by

$$\boldsymbol{v}_{\mathrm{GC}} = \mu \frac{\boldsymbol{B} \times \nabla \boldsymbol{B}}{qB^2} + \frac{\boldsymbol{E} \times \boldsymbol{B}}{B^2}, \tag{2}$$

where μ is the first adiabatic invariant. The first term is the gradient B drift, which causes the particle to drift azimuthally about the Earth along trajectories of constant magnetic field strength, and the second term is the $\mathbf{E} \times \mathbf{B}$ drift, which allows particles to be transported to regions of stronger or weaker magnetic field. We have neglected the additional drift term related to the curvature of the magnetic field line because we are only modeling equatorially mirroring particles.

Drift paths for two electrons with $\mu = 20$ MeV/G under the influence of a uniform dawn-to-dusk 2 mV/m electric field for 30 min are shown in Figure 9. The electrons are initialized at $L = 3$ for 06 magnetic local time (MLT) and 18 MLT. In the absence of an electric field, both electrons would drift counterclockwise along the dashed line at $L = 3$. The dawn-to-dusk electric field introduces a sunward drift that causes the electron on the nightside to move radially inward, while the electron on the dayside moves radially outward. Although the electric field is uniform, the dayside electron experiences ~0.5 L outward transport, and the nightside electron moves inward by only ~0.3 L. This asymmetry is due to the $1/L^3$ dependence of the magnetic field, which causes the $\mathbf{E} \times \mathbf{B}$ drift to be faster at larger L shells for a given electric field. For a purely azimuthal electric field, the $\mathbf{E} \times \mathbf{B}$ drift velocity reduces to

$$v_{E \times B} = \frac{E}{B}. \tag{3}$$

Due to conservation of the first adiabatic invariant, the inward transport on the nightside causes an increase in energy from ~190 to 250 keV, while the outward transport on the dayside results in a loss of energy from ~190 to 130 keV. Under the influence of a large-scale electric field, some of the particles on a given drift shell will gain energy, and others will lose energy. However, only a fraction of the particles need to move inward and be energized to create a large increase in flux given the steep radial PSD gradients in the inner magnetosphere.

In order to model the evolution of PSD profiles, we simulate 5808 electrons evenly spaced by 0.05 L and 0.5 MLT between $L = 2$ and 8. Each simulation models electrons of constant μ, and the PSD profiles are obtained by binning simulated particles by L shell and applying a weight based on the initial PSD profile. The weighting function is given by

$$W = f_0 \frac{L_0 * \mathrm{d}L_0 * \mathrm{dMLT}_0}{L_f * \mathrm{d}L_{\mathrm{bin}} * \mathrm{dMLT}_{\mathrm{bin}}} \tag{4}$$

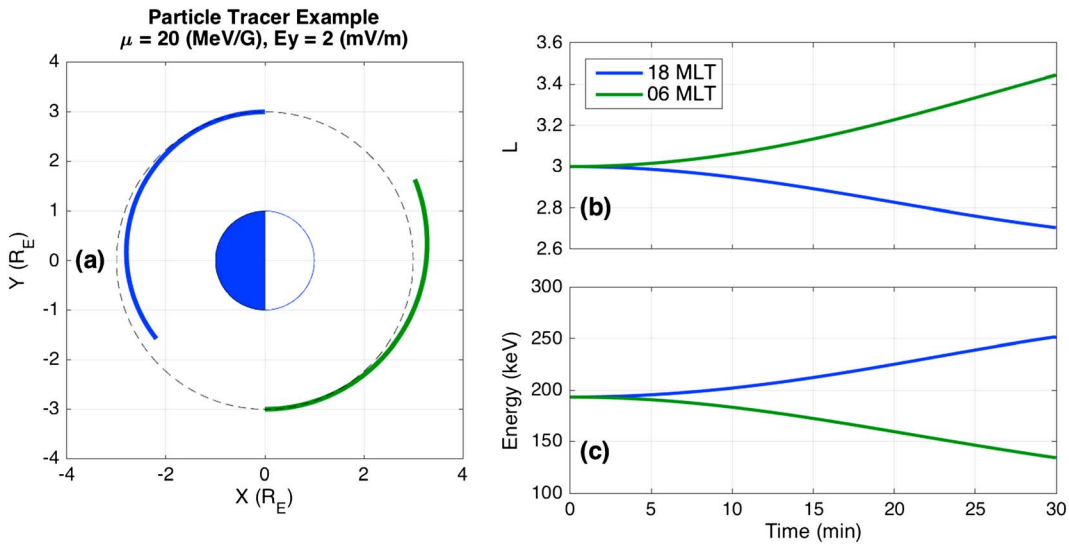

Figure 9. Trajectories for equatorially mirroring electrons with $\mu = 20$ MeV/G under the influence of a 2 mV/m uniform dawn-to-dusk electric field for 30 min. (a) Electron positions in the equatorial plane and time evolution of (b) L shell and (c) energy.

where f_0 is the initial PSD applied to the particle, L_0 is the initial L shell, L_f is the final L shell, dL_0 and $dMLT_0$ are the initial L and MLT spacing of simulated particles, and dL_{bin} and $dMLT_{bin}$ are the widths of the L and MLT bins. The ratio of the initial to final L shell accounts for the fact that simulated particles at larger radial distances represent proportionally more real particles given that the simulated particles are distributed on a uniform (L and MLT) grid.

The initial distributions are assumed to be symmetric in local time, and the final PSD profiles are averaged across all local times. We used PSD data from the two passes shown in Figure 5 to simulate the evolution of PSD under the influence of a uniform 2 mV/m dawn-to-dusk electric field. Figure 10 (left column) compares the measured PSD profiles to the simulated profiles after the electric field has been applied for 13.5 min. The μ values range from 20 to 100 MeV/G, which translates to 190–690 keV at $L = 3$. This simple convection model matches the inward transport for 40–100 MeV/G electrons, but it underpredicts the change in location of the steep radial gradient for 20 MeV/G electrons. We chose the 13.5 min simulation time to achieve the best match to the observed PSD profiles.

An important consideration for interpreting these results is the drift period of the electrons relative to the duration of the applied electric field. A given particle will experience no net radial transport under the influence of a large-scale electric field for exactly the drift period—the particle may move radially inward or outward during the drift orbit, but it will return to the initial position after one complete orbit if the electric field is constant. At a given L shell, higher-energy electrons drift faster due to the μ dependence of the gradient B drift.

$$v_{\nabla B} = \mu \frac{B \times \nabla B}{qB^2}. \tag{5}$$

Figure 11 shows drift periods for different μ values as a function of L shell. Near $L = 3$, 40 MeV/G electrons have a drift period of roughly 1 h and 100 MeV/G electrons drift in about 30 min. The drift periods begin to increase sharply for $\mu < 40$ MeV/G.

A possible explanation for the discrepancy for lower μ values is that a low-amplitude electric field persisted for a long duration in addition to a shorter 2 mV/m enhancement. Due to the energy-dependent drift periods, the lower energy electrons would be influenced by the long-duration electric field, and the faster-drifting, more energetic electrons would not be affected. Figure 10 (right column) shows the simulation results for a 0.5 mV/m electric field applied for 54 min followed by a 2 mV/m electric field for 13 min. The steady, low-amplitude convection electric field created net inward transport for 20 MeV/G electrons, but the shorter drift period for 40–100 MeV/G electrons led to little net transport until the 2 mV/m electric field was applied. The combination of these two effects is able to match the observed transport for $\mu = 20$–100 MeV/G.

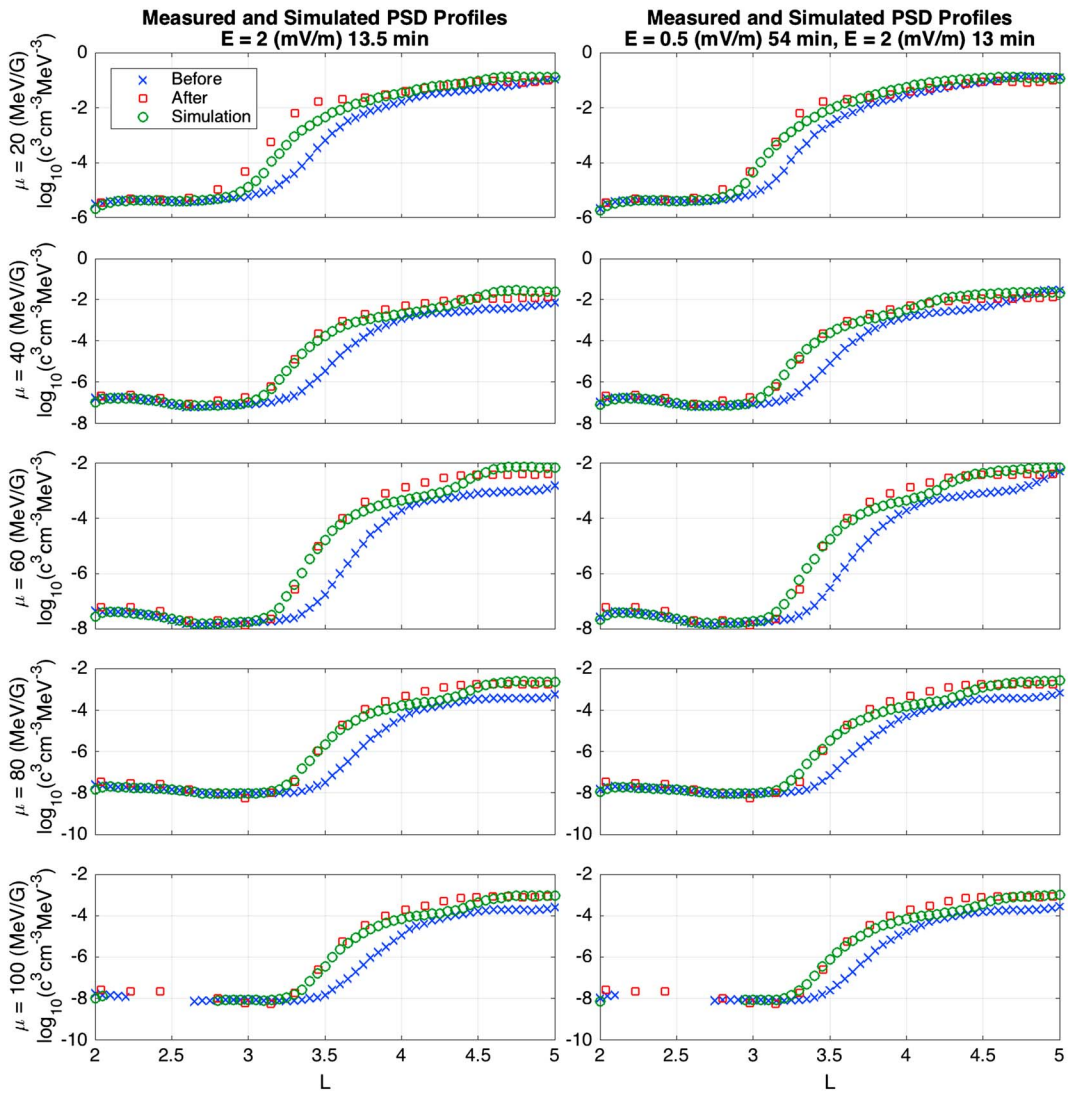

Figure 10. Observed PSD profiles and a simulation for a uniform 2 mV/m dawn-to-dusk electric field applied for (left column) 13.5 min and a 0.5 mV/m electric field applied for 54 min followed by a 2 mV/m electric field applied for (right column) 13 min.

After achieving a solution that matched electrons with $\mu = 20$–100 MeV/G, we extended the simulation to higher μ values to test where this simple model breaks down. Using MagEIS data only, we were able to produce PSD profiles up to 400 MeV/G that covered a large enough L range to observe the differential movement of the sharp PSD gradient between passes. $\mu = 400$ MeV/G corresponds to 1.3 MeV at $L = 3.5$. The results for 100–400 MeV/G electrons are shown in Figure 12 under the influence of a 2 mV/m dawn-to-dusk electric field applied for 13 min. The previous results in Figure 10 show that the long-duration 0.5 mV/m electric field had little effect on electrons above $\mu = 40$ MeV/G, so we only focus on the impact of the larger-amplitude electric field.

The results from the simple convection model begin to diverge from the observations at $\mu = 200$ MeV/G, and the $\mu = 400$ MeV/G electrons are barely affected by this electric field. This can be understood by the drift periods in Figure 11: electrons with μ greater than 200 MeV/G at $L = 3$ drift around the Earth in less than 25 min, and the electric field was applied for 13 min, which is a significant fraction of the drift period. Large-scale electric fields applied for an entire drift period have zero net effect on radial transport for a given particle. These results suggest that shorter-duration electric field enhancements would be required to match the observed behavior of higher-energy electrons. Close inspection of the electric field data show variations

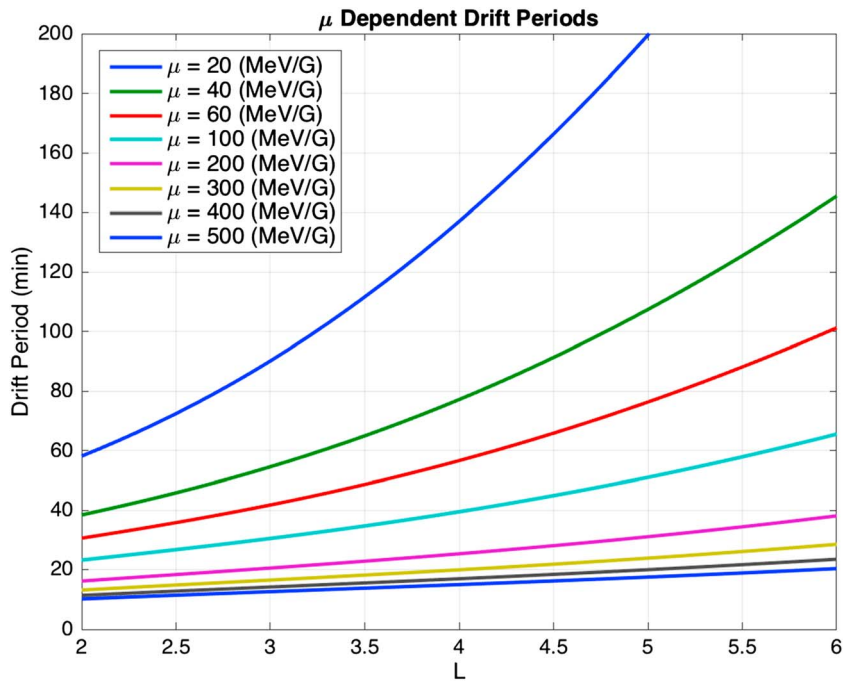

Figure 11. Drift periods as a function of L shell for constant μ electrons.

of 0.5–1 mV/m on timescales of 2–3 min, which may explain the observed transport for higher-energy electrons. Alternatively, the disagreement for higher energies may indicate a transition point where ULF waves or local acceleration become important.

6. Discussion

The results in the previous section show that the evolution of electrons over a wide range of energies (~130–500 keV) at low L shells in the slot region can be explained by radial transport through a simple, uniform, large-scale convection electric field model. In situ electric field measurements by the Van Allen Probes and THEMIS E support the picture that the convection electric field penetrated to low L shells during this event. Electric fields were measured by all three spacecraft on the order of 1–2 mV/m below $L = 3$. Also, the plasmapause is known to be driven by large-scale electric fields, and gradients in spacecraft potential as well as boundaries for plasmaspheric hiss and chorus suggest that the plasmapause moved inward to below $L = 2$ during this period. The simulation demonstrates that the same large-scale electric fields responsible for altering the shape of the plasmasphere are also capable of transporting 100s keV electrons radially inward, creating the observed electron flux enhancements.

The duration of the applied electric field creates a differential effect on electrons of different energies due to the energy-dependent drift periods of the electrons. This concept is analogous to drift resonance with ULF waves, which is used to explain radial diffusion for MeV electrons. However, the physical interpretation is fundamentally different: ULF waves are interpreted as resonant oscillations at particular frequencies determined by the magnetic field and plasma populations, but convection is a large-scale sunward flow driven by the solar wind; ULF oscillations are zero mean, but the convection electric field has a net DC component pointing from dawn to dusk. The simulated 2 mV/m electric field enhancement for 13 min could be viewed as a ULF wave with a frequency of 1.2 mHz, but physically, it represents short-duration increase of sunward flow in the inner magnetosphere.

This model is also differentiated from radial diffusion by ULF waves because the transport occurs in a relatively large step over a short period of time. Although the complete filling of the slot region typically occurs over many hours, it is unclear based on the sparse spatial and temporal sampling from only two spacecraft whether the flux enhancements are a result of a series of impulsive steps or are due to a slow diffusive

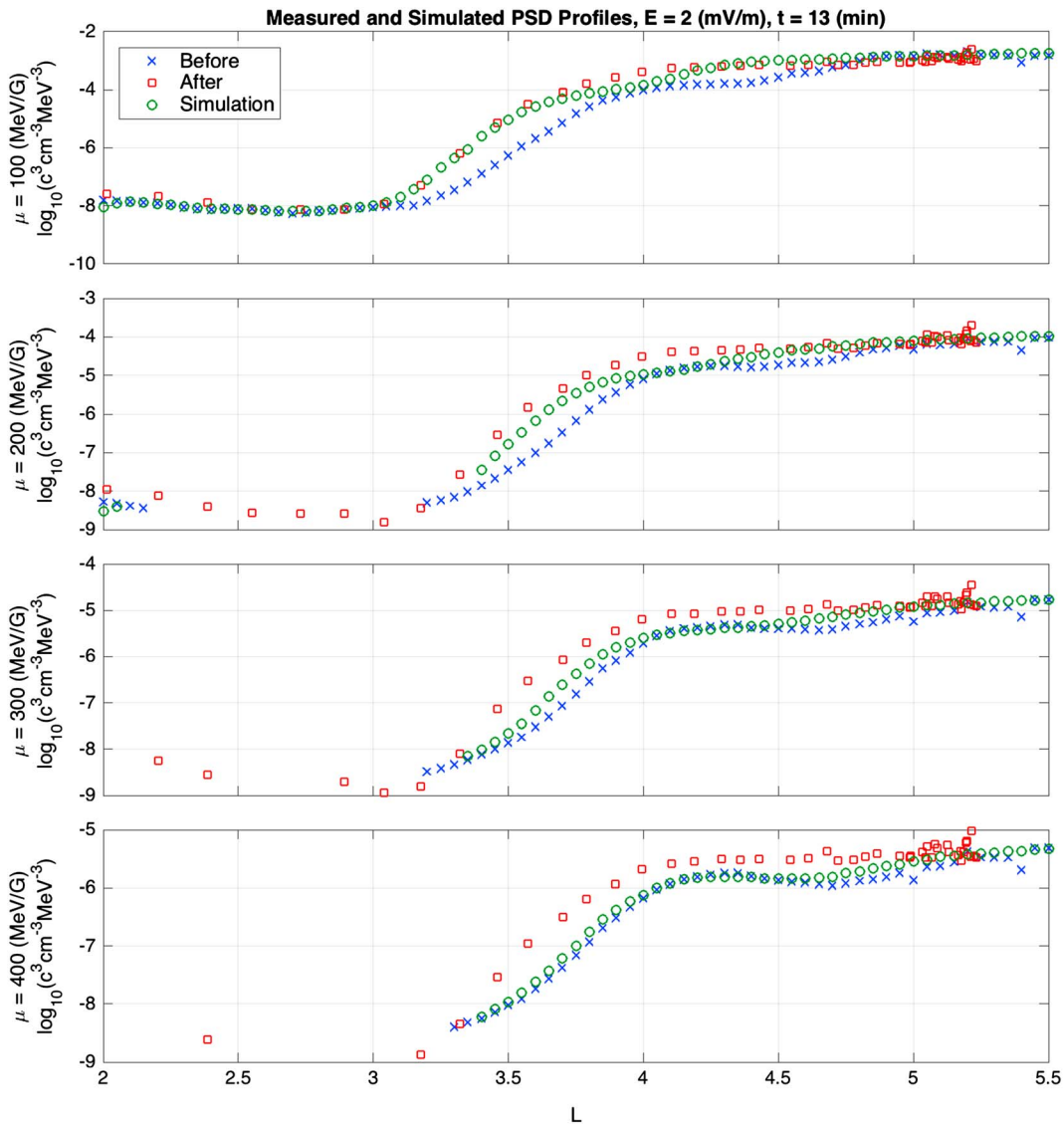

Figure 12. Observed PSD profiles and simulation results with a uniform 0.5 mV/m dawn-to-dusk electric field applied for 54 min, followed by a 2 mV/m dawn-to-dusk electric field applied for 13 min.

process. Our simple model using electric fields similar to the observations shows that the enhancements could be described by nondiffusive transport related to increases in the convection electric field.

The uniform convection model that matched the observed transport for 20–100 MeV/G electrons did not reproduce the behavior of the higher-energy electrons. There are several interpretations of this result. The actual large-scale electric field may vary on timescales faster than the simulated 13 min, which would allow the faster-drifting electrons to be affected. This may be more realistic given the 2–3 min electric field variations present in the data.

Also, the steep PSD gradient is located at higher L shells for higher energies, so there may be fluctuations that are better described as ULF waves, rather than convection, which interact with the higher-energy electrons through conventional radial diffusion at these radial distances. The electric field measurements often exhibit more steady characteristics at lower L shells and increased variation at higher L shells (Figures 6–8).

Local acceleration may also explain the electron dynamics for both the lower and higher ends of the energy range under study. The broadband wave power below ~100 Hz observed by the Van Allen Probes (Figures 7d and 7e) is an indication of kinetic Alfvén waves, which are often observed in the inner magnetosphere during

geomagnetically active times [e.g., *Malaspina et al*., 2014; *Chaston et al*., 2015]. These electric field structures can accelerate lower energy electrons (~100 eV) to keV energies, providing a seed population that can be further accelerated by the observed chorus waves through quasi-linear diffusion to 100–150 keV [*Ma et al*., 2016]. This process may explain the additional acceleration of 20 MeV/G electrons that was not reproduced by the single 2 mV/m enhancement in convection (Figure 10, left column).

The increase in flux occurring first for lower energies and then later at higher energies near $L = 3$–3.5 (Figure 4) is qualitatively consistent with quasi-linear diffusion through interaction with the observed chorus waves (Figure 7) [e.g., *Thorne et al*., 2013]. However, the timescale for acceleration by quasi-linear diffusion for 100s keV electrons is on the order of hours, and it increases to days for MeV electrons [*Horne et al*., 2005]. Our observations show 1–2 orders of magnitude flux enhancement for 900 keV electrons between $L = 3.5$–4 over 1.5 h. This rapid acceleration for higher energies might be achieved by nonlinear trapping by parallel chorus waves [e.g., *Albert*, 2002; *Artemyev et al*., 2015], which could accelerate 100s keV electrons to >1 MeV in less than 1 h [e.g., *Omura et al*., 2015].

While we cannot definitively distinguish between radial transport and local acceleration given the sparse spatial and temporal observations, the success of a simple convection model in matching the dynamics of 20–100 MeV/G (~190–700 keV at $L = 3$, ~130–500 keV at $L = 3.5$) electrons suggests that radial transport is the dominant energization mechanism for these energies. Also, the relative radial displacement of the steep PSD gradient was consistently ~0.3 L for electrons up to at least 400 MeV/G (Figure 12), and there were no peaks in PSD that would suggest local acceleration, even for the higher energies. Therefore, the PSD profiles alone do not clearly point to a transition between radial transport and local acceleration in this energy range.

7. Summary and Conclusions

This study focused on the relationship between large-scale electric fields and hundreds of keV electron enhancements in the slot region. The Van Allen Probes frequently observe slot region enhancements, and previous studies have shown that strong electric fields exist at low L shells during active times. We identified two consecutive dawnside passes by the Van Allen Probes separated by 1.5 h that show more than 2 orders of magnitude increase in hundreds of keV electron flux near $L = 3$. Converting flux to PSD revealed a sharp radial PSD gradient that moved radially inward between the two observations, suggesting radial transport as a mechanism. In situ electric field observations by the Van Allen Probes and THEMIS E provided direct evidence of 1–2 mV/m electric fields below $L = 3$ during the same time period. The presence of low L electric fields was also supported by spacecraft potential, plasmaspheric hiss, and chorus observations, which indicated that the plasmapause eroded below $L = 2$.

A 2-D guiding center particle tracer was developed to model the evolution of PSD under the influence of a uniform dawn-to-dusk electric field. We demonstrated that a 2 mV/m uniform convection electric field applied for 13.5 min could reproduce the observed changes in PSD profiles for 40–100 MeV/G electrons. However, the simulation did not produce enough inward transport to match the observations for 20 MeV/G electrons. We were able to resolve this discrepancy by applying a 0.5 mV/m electric field for 54 min prior to the 2 mV/m enhancement. The long-duration electric field was more effective in transporting the more slowly drifting low-energy electrons while having little effect on the higher energies, matching the observations for 20–100 MeV/G electrons.

We then applied the 2 mV/m uniform electric field to higher-energy electrons and found that same model could not explain the behavior for $\mu = 200$–400 MeV/G (~0.8–1.3 MeV at $L = 3.5$), which have drift periods of less than 25 min. This suggests that the actual electric field may have varied faster than the 13 min enhancement in the model, and the in situ electric field measurements do show variations on the order of 2–3 min. However, the presence of chorus waves in the same spatial region as the enhancements leaves the possibility open that local acceleration was at least partially responsible for the higher-energy electron dynamics.

Our results show that large-scale convection at low L shells with similar magnitude to the in situ measurements is sufficient to explain slot region enhancements for 130–500 keV electrons, and it is possible that variations in convection are important for even higher-energy electrons.

Acknowledgments
The work at the University of Colorado was mainly supported by funding through NASA Earth and Space Sciences Fellowship (NESSF) award NNX15AT57H and also partially supported by NASA grant NNX15AF56G. The authors thank the Van Allen Probes EFW, MagEIS, HOPE, and EMFISIS teams for providing data for this study. The Van Allen Probes MagEIS and HOPE data are publicly available at http://www.rbsp-ect.lanl.gov, the EFW data can be found at http://www.space.umn.edu/rbspefw-data, and the EMFISIS data are at http://emfisis.physics.uiowa.edu/data/index. Spin fit electric and magnetic field data for THEMIS can be found at http://themis.ssl.berkeley.edu/data/themis/tha/l2/fit, and OMNI data are located at http://cdaweb.gsfc.nasa.gov.

References

Albert, J. M. (2002), Nonlinear interaction of outer zone electrons with VLF waves, *Geophys. Res. Lett.*, *29*(8), 116–122, doi:10.1029/2001GL013941.

Artemyev, A. V., A. A. Vasiliev, D. Mourenas, A. I. Neishtadt, O. V. Agapitov, and V. Krasnoselskikh (2015), Probability of relativistic electron trapping by parallel and oblique whistler-mode waves in Earth radiation belts, *Phys. Plasmas*, *22*, 112903, doi:10.1063/1.4935842.

Blake, J. B., et al. (2013), The Magnetic Electron Ion Spectrometer (MagEIS) instruments aboard the Radiation Belt Storm Probes (RBSP) spacecraft, *Space Sci. Rev.*, *179*, 383–421, doi:10.1007/s11214-013-9991-8.

Bonnell, J. W., F. S. Mozer, G. T. Deloy, A. J. Hull, R. E. Ergun, C. M. Cully, V. Angelopoulos, and P. R. Harvey (2008), The Electric Field Instrument (EFI) for THEMIS, *Space Sci. Rev.*, *141*, 303–341, doi:10.1007/s11214-008-9469-2.

Califf, S., et al. (2014), THEMIS measurements of quasi-static electric fields in the inner magnetosphere, *J. Geophys. Res. Space Physics*, *119*, 9939–9951, doi:10.1002/2014JA020360.

Califf, S., X. Li, R. A. Wolf, H. Zhao, A. N. Jaynes, F. D. Wilder, D. M. Malaspina, and R. Redmon (2016), Large-amplitude electric fields in the inner magnetosphere: Van Allen Probes observations of subauroral polarization streams, *J. Geophys. Res. Space Physics*, *121*, 5294–5306, doi:10.1002/2015JA022252.

Carpenter, D. L., B. L. Giles, C. R. Chappell, P. M. E. Décréau, R. R. Anderson, A. M. Persoon, A. J. Smith, Y. Corcuff, and P. Canu (1993), Plasmasphere dynamics in the duskside bulge region: A new look at an old topic, *J. Geophys. Res.*, *98*(A11), 19,243–19,271, doi:10.1029/93JA00922.

Chaston, C. C., J. W. Bonnell, J. R. Wygant, C. A. Kletzing, G. D. Reeves, A. Gerrard, L. Lanzerotti, and C. W. Smith (2015), Extreme ionospheric ion energization and electron heating in Alfvén waves in the storm time inner magnetosphere, *Geophys. Res. Lett.*, *42*, 10,531–10,540, doi:10.1002/2015GL066674.

Darrouzet, F., J. De Keyser, P. M. E. Decreau, F. El Lemdani-Mazouz, and X. Vallieres (2008), Statistical analysis of plasmaspheric plumes with Cluster/WHISPER observations, *Ann. Geophys.*, *26*, 2403–2417, doi:10.5194/angeo-26-2403-2008.

Elkington, S. R., M. K. Hudson, and A. A. Chan (2003), Resonant acceleration and diffusion of outer zone electrons in an asymmetric geomagnetic field, *J. Geophys. Res.*, *108*(A3), 1116, doi:10.1029/2001JA009202.

Funsten, H., et al. (2013), Helium, Oxygen, Proton, and Electron (HOPE) mass spectrometer for the Radiation Belt Storm Probes mission, *Space Sci. Rev.*, *179*, 1–62, doi:10.1007/s11214-013-9968-7.

Goldstein, J., B. R. Sandel, M. R. Hairston, and P. H. Reiff (2003), Control of plasmaspheric dynamics by both convection and sub-auroral polarization stream, *Geophys. Res. Lett.*, *30*(24), 2243, doi:10.1029/2003GL018390.

Green, J. C., and M. G. Kivelson (2004), Relativistic electrons in the outer radiation belt: Differentiating between acceleration mechanisms, *J. Geophys. Res.*, *109*, A03213, doi:10.1029/2003JA010153.

Horne, R. B., R. M. Thorne, S. A. Glauert, J. M. Albert, N. P. Meredith, and R. R. Anderson (2005), Timescale for radiation belt electron acceleration by whistler mode chorus waves, *J. Geophys. Res.*, *110*, A03225, doi:10.1029/2004JA010811.

Kletzing, C. A., et al. (2013), The Electric and Magnetic Field Instrument Suite and Integrated Science (EMFISIS) on RBSP, *Space Sci. Rev.*, *179*, 127–181, doi:10.1007/s11214-013-9993-6.

Kurth, W. S., S. De Pascuale, J. B. Faden, C. A. Kletzing, G. B. Hospodarsky, S. Thaller, and J. R. Wygant (2015), Electron densities inferred from plasma wave spectra obtained by the waves instrument on Van Allen Probes, *J. Geophys. Res. Space Physics*, *120*, 904–914, doi:10.1002/2014JA020857.

Li, X., I. Roth, M. Temerin, J. R. Wygant, M. K. Hudson, and J. B. Blake (1993), Simulation of the prompt energization and transport of radiation belt particles during the March 24, 1991 SSC, *Geophys. Res. Lett.*, *20*(22), 2423–2426, doi:10.1029/93GL02701.

Lyons, L. R., and R. M. Thorne (1973), Equilibrium structure of radiation belt electrons, *J. Geophys. Res.*, *78*(13), 2142–2149, doi:10.1029/JA078i013p02142.

Ma, Q., D. Mourenas, A. Artemyev, W. Li, R. M. Thorne, and J. Bortnik (2016), Strong enhancement of 10–100 keV electron fluxes by combined effects of chorus waves and time domain structures, *Geophys. Res. Lett.*, *43*, 4683–4690, doi:10.1002/2016GL069125.

Malaspina, D. M., L. Andersson, R. E. Ergun, J. R. Wygant, J. W. Bonnell, C. Kletzing, G. D. Reeves, R. M. Skoug, and B. A. Larsen (2014), Nonlinear electric field structures in the inner magnetosphere, *Geophys. Res. Lett.*, *41*, 5693–5701, doi:10.1002/2014GL061109.

Malaspina, D. M., J. R. Wygant, R. E. Ergun, G. D. Reeves, R. M. Skoug, and B. A. Larsen (2015), Electric field structures and waves at plasma boundaries in the inner magnetosphere, *J. Geophys. Res. Space Physics*, *120*, 4246–4263, doi:10.1002/2015JA021137.

Omura, Y., Y. Miyashita, M. Yoshikawa, D. Summers, M. Hikishima, Y. Ebihara, and Y. Kubota (2015), Formation process of relativistic electron flux through interaction with chorus emissions in the Earth inner magnetosphere, *J. Geophys. Res. Space Physics*, *120*, 9545–9562, doi:10.1002/2015JA021563.

Reeves, G. D., et al. (2013), Electron acceleration in the heart of the Van Allen radiation belts, *Science*, *341*(6149), 991–994, doi:10.1126/science.1237743.

Reeves, G. D., et al. (2016), Energy dependent dynamics of keV to MeV electrons in the inner zone, outer zone, and slot regions, *J. Geophys. Res. Space Physics*, *121*, 397–412, doi:10.1002/2015JA021569.

Rowland, D. E., and J. R. Wygant (1998), Dependence of the large-scale, inner magnetospheric electric field on geomagnetic activity, *J. Geophys. Res.*, *103*, 14,959–14,964, doi:10.1029/97A03524.

Selesnick, R. S., Y.-J. Su, and J. B. Blake (2016), Control of the innermost electron radiation belt by large-scale electric fields, *J. Geophys. Res. Space Physics*, *121*, 8417–8427, doi:10.1002/2016JA022973.

Shprits, Y. Y., D. A. Subbotin, N. P. Meredith, and S. R. Elkington (2008), Review of modeling of losses and sources of relativistic electrons in the outer radiation belt II: Local acceleration and loss, *J. Atmos. Sol. Terr. Phys.*, *70*(14), 1694–1713, doi:10.1016/j.jastp.2008.06.014.

Su, Y.-J., R. S. Selesnick, and J. B. Blake (2016), Formation of the inner electron radiation belt by enhanced large-scale electric fields, *J. Geophys. Res. Space Physics*, *121*, 8508–8522, doi:10.1002/2016JA022881.

Thaller, S. A., et al. (2015), Van Allen Probes investigation of the large-scale duskward electric field and its role in ring current formation and plasmasphere erosion in the 1 June 2013 storm, *J. Geophys. Res. Space Physics*, *120*, 4531–4543, doi:10.1002/2014JA020875.

Thorne, R. M., Y. Y. Shprits, N. P. Meredith, R. B. Horne, W. Li, and L. R. Lyons (2007), Refilling of the slot region between the inner and outer electron radiation belts during geomagnetic storms, *J. Geophys. Res.*, *112*, A06203, doi:10.1029/2006JA012176.

Thorne, R. M., et al. (2013), Rapid local acceleration of relativistic radiation-belt electrons by magnetospheric chorus, *Nature*, *504*(7480), 411–414, doi:10.1038/nature12889.

Tsyganenko, N. A., and M. I. Sitnov (2005), Modeling the dynamics of the inner magnetosphere during strong geomagnetic storms, *J. Geophys. Res.*, *110*, A03208, doi:10.1029/2004JA010798.

Turner, D. L., et al. (2015), Energetic electron injections deep into the inner magnetosphere associated with substorm activity, *Geophys. Res. Lett.*, *42*, 2079–2087, doi:10.1002/2015GL063225.

Wygant, J., et al. (2013), The electric field and waves instruments on the Radiation Belt Storm Probes mission, *Space Sci. Rev.*, *179*(1–4), 183–220, doi:10.1007/s11214-013-0013-7.

Zhao, H., X. Li, J. B. Blake, J. F. Fennell, S. G. Claudepierre, D. N. Baker, A. N. Jaynes, and D. M. Malaspina (2014), Characteristics of pitch angle distributions of hundreds of keV electrons in the slot region and inner radiation belt, *J. Geophys. Res. Space Physics*, *119*, 9543–9557, doi:10.1002/2014JA020386.